ANALYSIS OF FLOW PHENOMENA WITHIN THE SIDE CHANNEL OF A REGENERATIVE PUMP BY MEANS OF HS- SPIV AND POD

Philipp Mattern, Martin Gabi
Institute of fluid machinery (FSM)
Karlsruhe Institute of Technology (KIT)

Jochen Kriegseis
Institute of Fluid Mechanics (ISTM)
Karlsruhe Institute of Technology (KIT)

ABSTRACT

To understand the complex flow phenomena within a regenerative pump, the side channel of a generic model with a diameter of 200 mm is examined by means of Highspeed- Stereo Particle Image Velocimetry (HS SPIV). It is shown, that by analyzing the data using a proper orthogonal decomposition (POD) and subsequently a common-base proper orthogonal decomposition (CPOD) significantly deeper understanding of the complex flow within the machine can be achieved compared to the classic approach of time and spatial averaging. The strong influence of the all-concealing average flow can be minimized as well as blade related flow patterns can be revealed. Conclusive it is shown, that the primary dynamic of the flow through the machine for different operating points (OPs) can be reduced to only a few dominant structures.

INTRODUCTION

Regenerative pumps are characterized by very high specific pressure heads and low specific flow rates. As such, they cover a special field of application, which to date has been rarely documented in public literature. They are self-priming and their working principle is "quasi multistage". Since their efficiency is relatively low compared to the more common axial or radial types, advanced optimization strategies are of utmost importance for the development of such
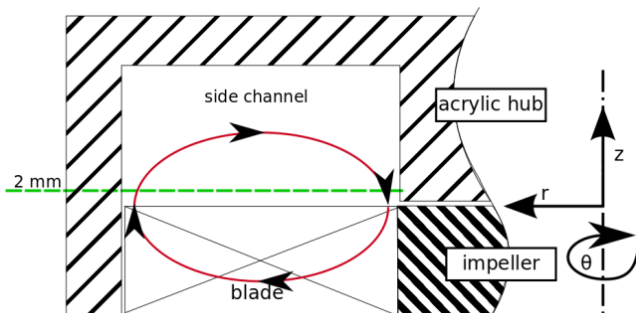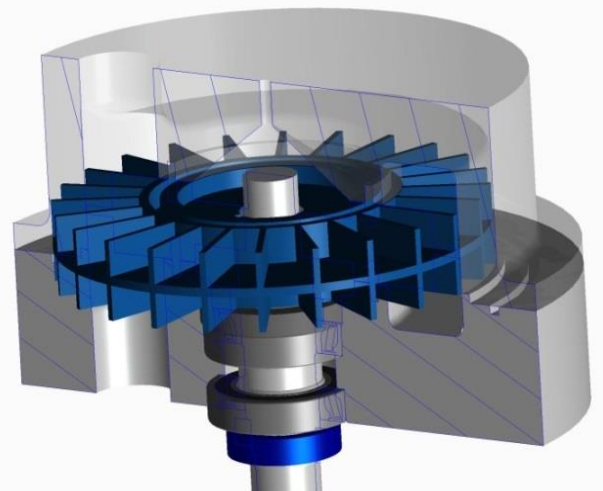

Figure 2: CAD Model of the regenerative pump

pumps. The basic working principle of the machine is described by the so called "circulation theory", which is based on the Euler equation for fluid machinery. The transport mechanism behind that is described by an axial interaction between the flow in the side channel and the blades of the impeller (secondary flow). This secondary flow is shown in red in Figure 1. As such, characterization of the helicoidal flow structure interacting between the impeller and the side channel provides a deeper inside into the involved cause-effect-relations. In addition, as for most fluid machinery, different OPs lead to a strong alteration of the flow field within the machine, making it even more difficult to describe the flow behavior. The purpose of the present study therefore addresses the identification of the coherent flow patterns in game. In order to obtain the desired flow information, a generic model (Figure 2) with full optical accessibility has been designed and integrated in a classic pump test rig to enable a detailed examination by means of HS SPIV. Although 5 Measurement planes with respect to the impeller were captured, only the 2mm Plane nearest to the impeller (see Figure 1) is discussed in this paper, as the most sigificant topologic differences can be observed in this

Figure 1: Measurement planes (dotted green) with superimposed secondary flow (red)

plane.. Basis of disscussion are 3 extremly different OPs distributed along the characteritic curve of the pump. Two being at the extrema, as well as 1 in the region of the optimal point (Figure 3).

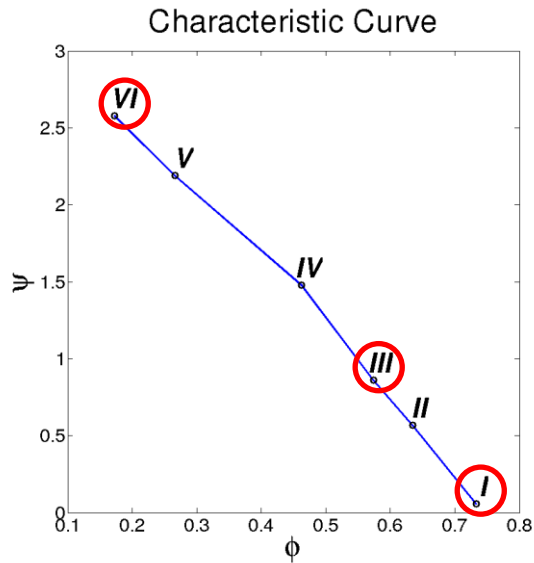

Figure 3: Characteristic Curve with discussed Operating Points marked in red

EXPERIMENTAL SETUP

The impeller of the pump with its 24 blades on each side is covered by an acrylic casing with the side channel integrated. Although a double flow machine was realized due to symmetrical reasons, only the upper flow was examined. The machine is running at a speed of 500 rpm. The classic layout of the test rig allows full control over the flow re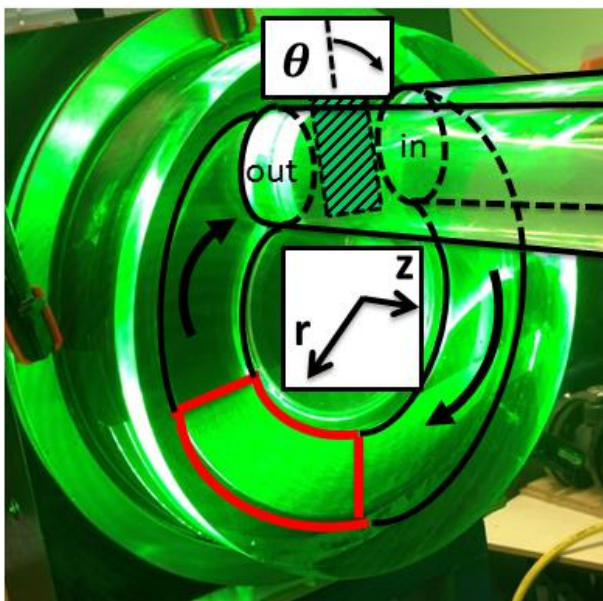gime and therefore the operating point of the machine. An iterative process regarding feasibility and measurability led to the final design. As optical accessibility was the main criteria, most surfaces were designed planar, curvatures were reduced to a minimum and angles were designed to be close to a square angle. To illustrate the flow through the machine, Figure 4 is introduced. The fluid enters the machine at the upper right corner and is circularly transported along θ through the side channel to the outlet (This defines the main flow). θ and r are defined in cylindrical coordinates, with z defining the axial coordinate. Note that in- and outlet are separated by a stripper (hatched Area), which is used as the origin of the circumferential coordinate θ. The light sheet of the Laser enters the acrylic casing from the left side and illuminates the area marked in red. It can be assumed, that the flow at this position is already fully developed The Stereo PIV System is set up in a standard Forward/Backward scattered Setup, with an angle of 65° between both cameras and a distance of 340 mm between the cameras and the light sheet. The flow is captured at 2000 fps with a resolution of 1 Megapixel. More details of the experimental setup can be found in Mattern et $al.$ (2014).

POST PROCESSING

For PIV Analysis PIVTEC's PIVview (V3.5.9.1) is used. Common methods of dewarping and disparity correction are applied. The cross correlation has an interrogation area of 16x16 pixels and an overlap of 50%. A strict dynamic mean filter of 2*mean velocity $\pm$ 1*standard deviation leads to a small amount of around 0.5% invalid vectors which could nearly all be replaced by their second highest correlation peaks. Separation Time (Pulse Distance) between the two pulses is 100 µs. During 1.4 seconds of measurement, N =2771 velocity maps for an area of 110x50 mm each containing around 3000 three component vectors are captured. Customized post-processing Algorithms have been applied for any further analysis of the velocity data.

Figure 4: Acrylic Side Channel with marked PIV Measurement Position (red area)

AVERAGED RESULTS

In a first approach the resulting vector maps are time averaged. Figure xxx shows this exemplarily for the 3 different OPs. In order to identify regions of high fluctuation, the root-mean-square (RMS) velocity fluctuation is given as well in Figure XXX. As for all following figures, the black lines represent the walls of the side channel. Due to refraction and blockage the field of view was limited. It is clearly visible, that the average in-plane velocity (of 3 m/s), as well as the axial component is changing significantly while moving from high (top) to low (bottom) volume flows. While being in overload mode *(OP I)* (top), the fluid is mainly pushed through the side-channel with only a minor interaction between the side-channel and the impeller. Close to its optimal operating point *(OP III)*, the in-plane velocity is evenly distributed along the radius. In part load mode *(OP VI)* the flow field changes notably, with backflow against the rotational direction of the impeller and distinct vortices being present. A dashed red line marks the zero-crossing: It is remarkable, that for all OPs, the axial velocity component is only positiv for a small region at the outer rim; a region of strong fluctuation, as shown

by the RMS Figures. These high positive axial velocities can be explained by centrifugal forces guiding the fluid in a radial direction. As the fluid is blocked by the casing, it cannot be transported furthermore along the radius and therefore has to evade to the only direction left (upwards into the side channel). The necessary negative backflow into the blade channel is now more obvious.

MODAL ANALYSIS (POD/CPOD)

In order to uncover coherent structures embedded in the flow, the data was decomposed by means of proper orthogonal decomposition (POD). A brief introduction into POD and its' common-base extension (CPOD) is provided below, adapted from Kriegseis *et al.* (2010) and Fernando *et al.* (2014).

Unsteady velocity information $\tilde{U}(\vec{x}, t)$ can be decomposed into its average and transient components, as shown in the Reynolds decomposition $\tilde{U}(\vec{x}, t^i) = \bar{u}(\vec{x}) + u(\vec{x}, t^i)$ for time step t^i. In general, a POD separates spatially correlated but temporally inhomogeneous flow structures from uncorrelated random fluctuations (noise), both of which are contained in the deviations $u(\vec{x}, t^i)$. These deviations u^i from the
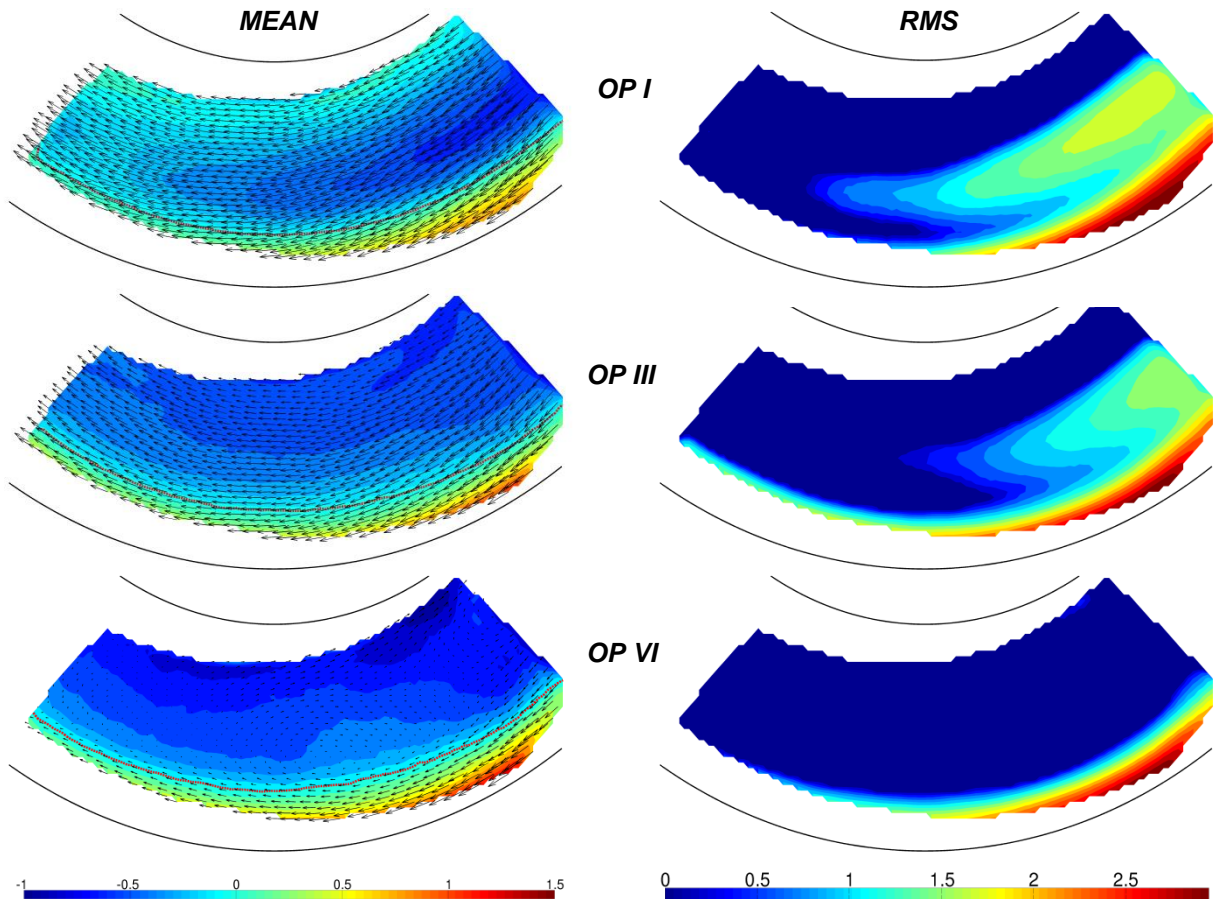

Figure 5: Time averaged velocities (left) with their corresponding RMS velocity fluctuations (right) for 3 OPs

mean form a covariance matrix $R = UU^T$, where $U = [u^1, u^2 \dots u^N]$. The solution of the eigenvalue problem $R\Phi = \lambda\Phi$ leads to the POD Modes ϕ_j (eigenvectors) with corresponding eigenvalues λ_j. These Modes in fact reveal coherent flow patterns superimposed to the mean flow field.

The resulting contribution of each mode j to the overall signal power is given by $P_j = \lambda_j / \|\lambda\|$. Since the eigenvalues are ordered decreasingly, the first few Modes ϕ_j of the matrix $\Phi = [\phi_1, \phi_2 \dots \phi_N]^T$ typically contain the main part of the energy in the recorded flow scenario. The impact of each Mode ϕ_j to the individual snap shots u^i can be determined in terms of the weighting coefficients $a_j^i = \phi_j u^i$. Note that the average $\overline{a_j}$ of a_j^i over N snapshots is zero by definition, i.e. $\overline{a_j} = \frac{1}{N}\sum_{i=1}^{N} a_j^i := 0$. In contrast, the standard deviations $\sigma_j = \sqrt{\frac{1}{N-1}\sum_{i=1}^{N}(a_j^i)^2}$ are non-zero and indicate the fluctuation intensity of Mode ϕ_j.

In cases where the research objective addresses the influence of parameter variations $k \in K$ (varying operating points *I-VI* in the present study), a direct comparison of the resulting modal structures seems promising. Due to the fact that different PODs lead to different (independent) eigenvalue problems, such a comparison is only valid on a phenomenological basis. A quantitative comparison of power contributions P_j and fluctuations σ_j is meaningless, since different base transformations have been performed. To overcome these shortcomings, all experiments have to be merged to a common basis, i.e. $U = [U^1, U^2 \dots U^K]$ respectively $U = [U^I, U^{II} \dots U^{VI}]$ for the present case. Consequently, the corresponding eigenvalue problem leads to flow patterns of global validity for the entire considered parameter space. Hence, a parameter-specific evaluation of the resulting coefficients a_j^i according to $\overline{a_{j,k}} = \frac{1}{N_k}\sum_{i=N_{k-1}+1}^{N_k} a_j^i$ and $\sigma_{j,k} = \sqrt{\frac{1}{N_k-1}\sum_{i=N_{k-1}+1}^{N_k}(a_j^i - \overline{a_{j,k}})^2}$ allows a quantitative comparison of the individual settings. Consequently, the impact of a particular flow pattern to the overall (parameter dependent) flow scenario can be quantified. Note that the sectional average $\overline{a_{j,k}}$ can differ from zero, which indicates a shift behavior of the respective flow patterns.

POD RESULTS

While Averaged RMS Figures help to identify regions of high fluctuation, POD Analysis is useful to characterize their structure and describe the underlying driving forces:

Figure 6 shows the first two modes of the three considered OPs. Modal patterns are shown as vectors for the in-plane and as contour plot for the
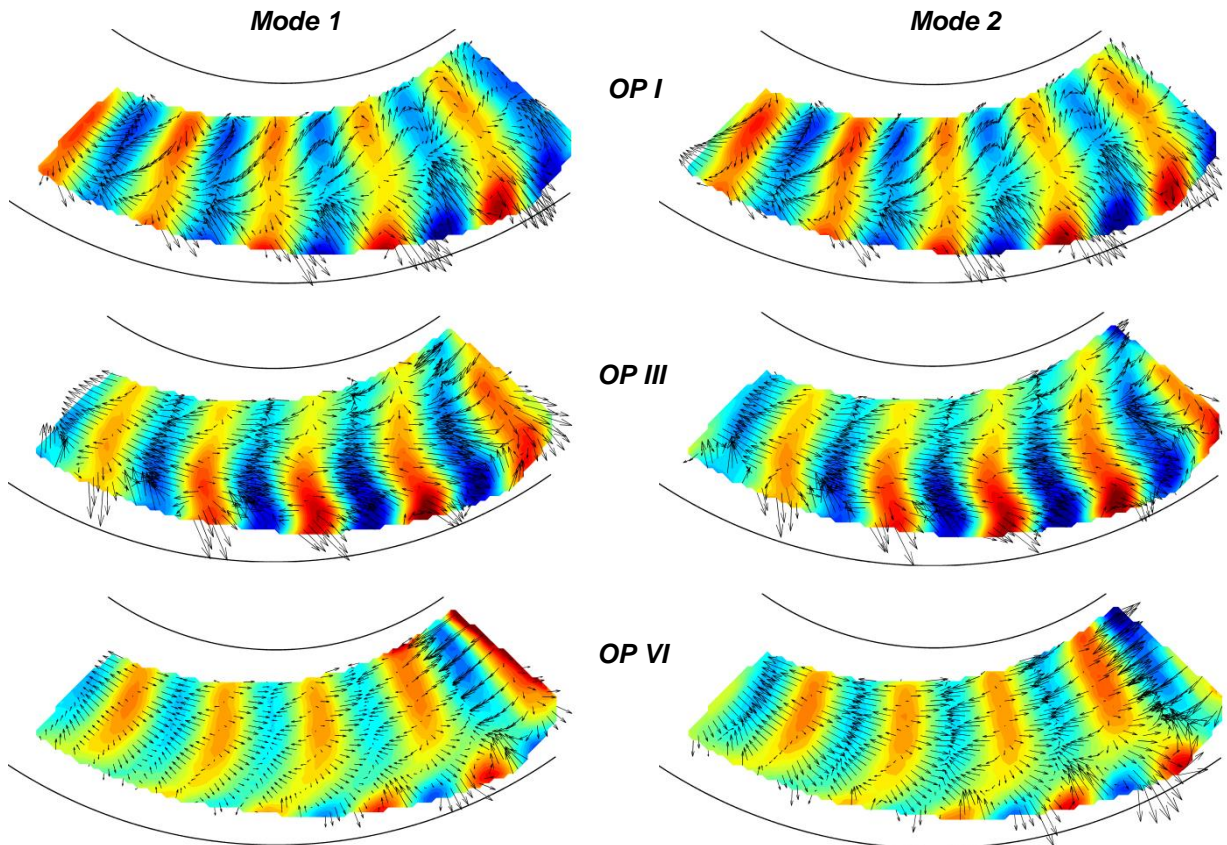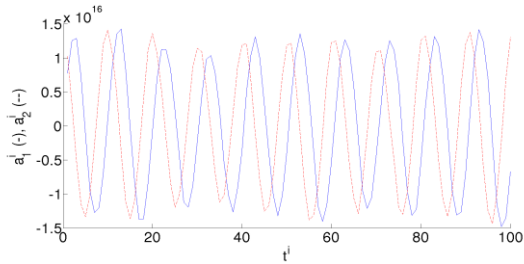

Figure 6: First and second Mode for the 3 OPs

Figure 7: Weighting coefficients Mode 1&2 *OP I*

out-of-plane component (with warm colors being positive). It is remarkable, that although the OPs are very different, the first two modes of all OPs, as well as their corresponding first harmonics (not shown in this paper), reveal very similar flow patterns. Both show blade related flow structures in plane, as well as out-of-plane; a system of interacting vortices can be observed at the outer diameter of the side channel. This system shows pairs of counter-rotating vortices, which are assumed to be the effect of the trailing edges of the blades interacting with the outer wall of the side channel (an exact interpretation is subject to further investigations). A distinct difference between Mode 1 and 2 is the fact, that the structures are shifted by a certain angle in flow direction. This 90°-phase shift becomes more obvious from the reconstructed coefficient of the respective modes, as shown in Figure 7. The coefficient oscillation reveals the
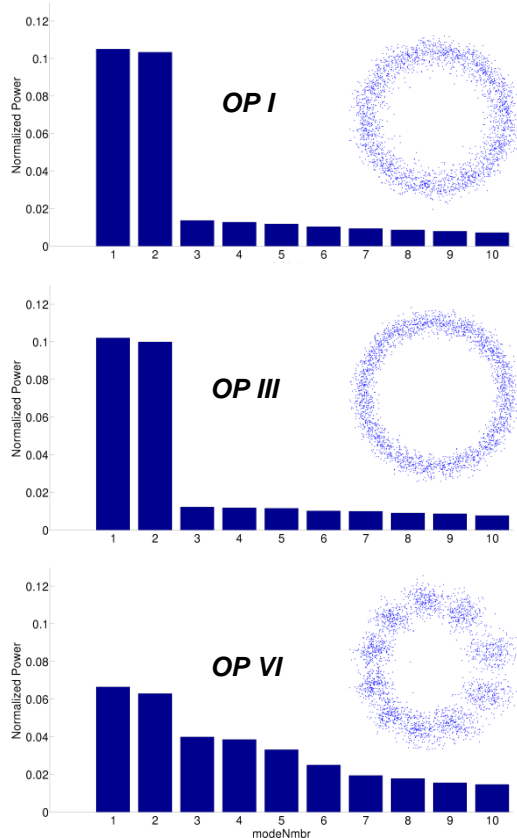
blade passing frequency of 200 Hz. Note that the 90°-phase shift at identical frequency is verified by the circular shape of the corresponding Lissajous figures (Figure 8). To quantify the influence of Modes 1 and 2, the normalized energy contribution of the 10 first Modes is given in Figure XXX. For *OP(I)* and *OP(III)*, the energy of the first two Modes are nearly half an order of magnitude higher than the rest. As all following Modes show no structures obviously related to any parameter of the machine and with their modal energies asymptotically approach a constant value, they are considered as statistically similar. This is a strong indicator for random noise. For part load mode *OP(VI)*, the influence of random noise is more severe as Mode 1 &2 are only slightly higher as the beginning noise.

In conclusion, a combination of Mode 1 and Mode 2 is already a good resemblance of the instantaneous turbulent flow field, containing about 20% of the flows fluctuation energy for the near-blade planes.

The similarities of the Modes lead to the preliminary conclusion that the dominant flow pattern is independent from the operating point. This hypothesis will be tested below:

CPOD

As mentioned before, the POD Results cannot be compared directly, as they share no common base. However, similar flow patterns are a good indicator, that a CPOD could reveal quantifiable similarities:

Figure 9 introduces the first 4 Modes from the CPOD, as well as Mode 9 &10. To understand the energy contribution of the OPs per Mode Figure 10 is shown. It describes the individual power contribution of every single operating point to the first 10 Modes.

Mode 1 (top left) shows a strong in-plane motion, with nearly no axial exchange (so-called Shift Mode). Weighted with a signed Coefficient, it either enforces *(OP I)* or weakens *(OP IV)* the dominant primary flow through the side-channel. (For a deeper understanding the reader is referred to Fernando et. al.) The strong character of the first Mode is enforced by the Power of the Mode, which is an order of magnitude higher than the remaining Modes.

Modes 2&3 show the blade dependent 90°-Shift Pattern already known from the single PODs. With this behavior shown in the CPOD, the previous hypothesis of an operating point independent primary flow is proven. Tendentially they show an increasing contribution to the power from overload to part load.

Mode 4 reveals a vortex structure in the upper right corner. Nonetheless. with its shape and power contribution it cannot be associated directly to a phenomena.
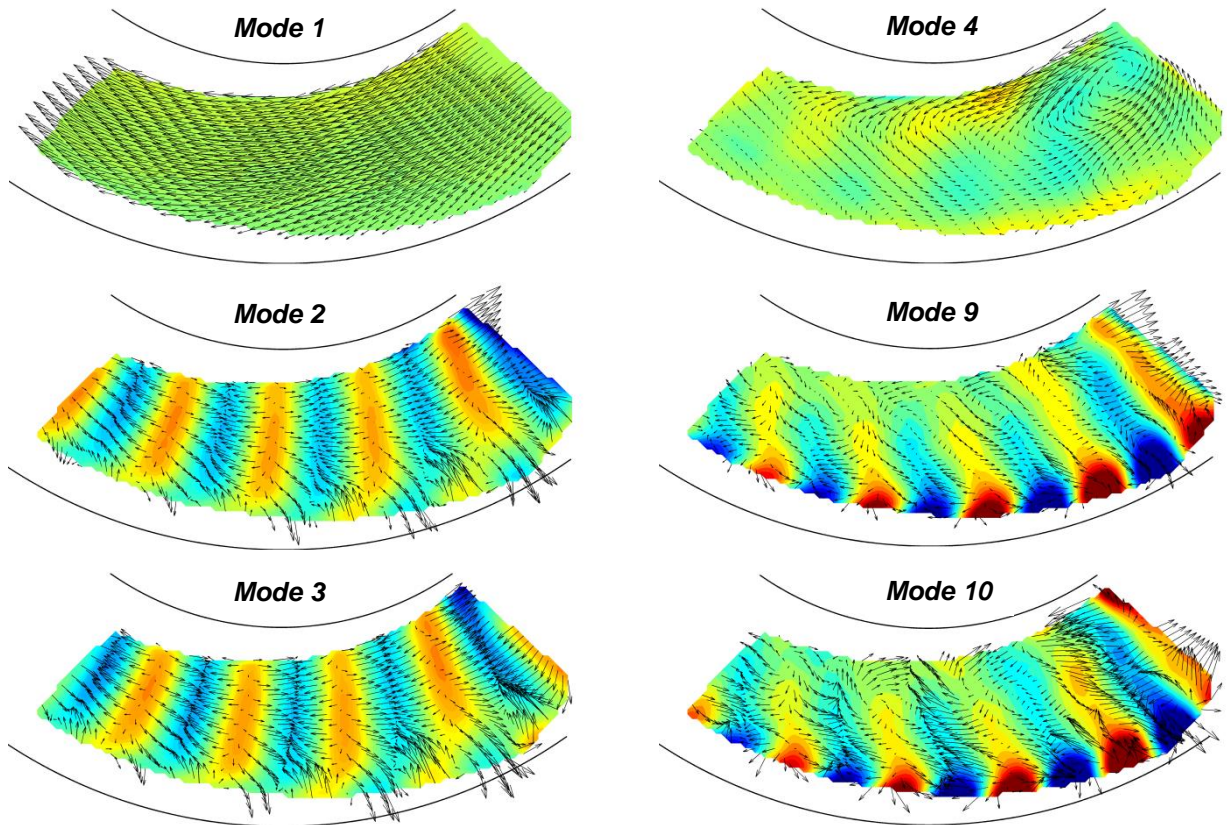

Figure 8: Power Distribution for the first 10 Modes and the Lissajous Figures for Mode 1&2

Figure 9: CPOD Modes

Mode 9&10 are showed exemplarily to give an idea about the first harmonics of Mode 2&3.

CONCLUSION

POD showed that a blade related flow structure was identifiable for the considered OPs.

Subsequently, by means of CPOD it could be proven, that the dominant primary flow dynamic is not depending on the operating point. Furthermore, the dominant flow dynamics can be attributed as blade-related.

Additionally, it revealed that random fluctuations, while increasing with the operating point moving towards part load mode, conceal the secondary flow characteristic, which is OP related.

As such, a common base analysis only provides limited insight into the OP specific development of the secondary vortical dynamic during operation. A further investigation of this dynamics is beyond the scope of the present work.

REFERENCES

Fernando, J.,Kriegseis, J., Rival, D., 2014. Modal analysis of confined square and rectangular cavity flows. Int. J. Heat Fluid Flow 47, 123-134

Kriegseis, J.,Dehler, T., Gnirß, M., Tropea, C., 2010. Common-base proper orthogonal decomposition (CPOD) as a means of quantitative data comparison. Meas. Sci. Technol. 21, 085403 (7pp)

Mattern, P., Gabi, M., Wagner, T., Boehle, M., 2014, Investigations in a side channel pump using high speed Stereo Particle Image Velocimetry, 15th Int. Symp. Transp. Phenom. Dyn. Rot. Machinery –ISROMAC-15
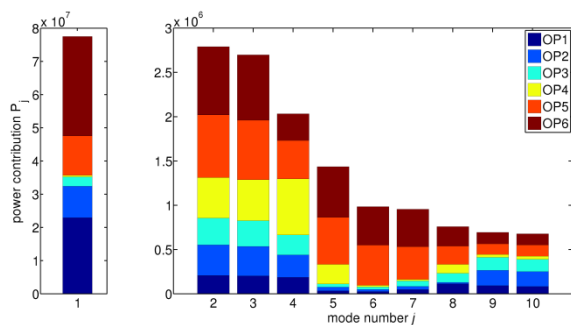

Figure 10: CPOD Power Distribution per OP for the first 10 Modes